Supplementary Information for: "Programmable spectral symmetries in an anisotropic quantum Rabi simulator"

Jia-Cheng Song,[1,2,*] Yu Liu,[1,†] Ming-Chuan Wang,[1,2,*] Ke-Xiong Yan,[3,*] Yang He,[1,2] Yun-Hao Shi,[4] Wei-Ping Yuan,[1,2] Cheng-Lin Deng,[5] Li Li,[1,2] Zhen-Ting Bao,[1,2] Yutao Chen,[1,2] Xu-Yang Gu,[1,2] Tian-Ming Li,[1,2] Gui-Han Liang,[1] Zheng-He Liu,[1,2] Wei-Guo Ma,[1,2] Zhen-Yu Peng,[1,2] Shuai-Li Wang,[1,2] Yong-Xi Xiao,[1,2] Yi-Han Yu,[1,2] Jia-Chi Zhang,[1,2] Kui Zhao,[5] Min-Xuan Zhou,[1,2] Kaixuan Huang,[5] Yu-Ran Zhang,[6] Yu-Xiang Zhang,[1,2,7] Zhongcheng Xiang,[1,2,7] Dongning Zheng,[1,2,7,8] Ye-Hong Chen,[3,9,‡] Kai Xu,[1,2,5,7,§] and Heng Fan[1,2,5,7,8,¶]

[1]*Beijing National Laboratory for Condensed Matter Physics, Institute of Physics, Chinese Academy of Sciences, Beijing 100190, China*
[2]*School of Physical Sciences, University of Chinese Academy of Sciences, Beijing 100049, China*
[3]*Fujian Key Laboratory of Quantum Information and Quantum Optics, College of Physics and Information Engineering, Fuzhou University, Fuzhou, Fujian 350108, China*
[4]*School of Physics, Xi'an Jiaotong University, Xi'an 710049, China*
[5]*Beijing Key Laboratory of Fault-Tolerant Quantum Computing, Beijing Academy of Quantum Information Sciences, Beijing 100193, China*
[6]*School of Physics and Optoelectronics, South China University of Technology, Guangzhou 510640, China*
[7]*Hefei National Laboratory, Hefei 230088, China*
[8]*Beijing Key Labratory of Advanced Quantum Technology, Beijing 100190, China*
[9]*Quantum Information Physics Theory Research Team, Center for Quantum Computing, RIKEN, Wako-shi, Saitama 351-0198, Japan*

(Dated: May 31, 2026)

CONTENTS

* These authors contributed equally to this work.
† yuliu@iphy.ac.cn; These authors contributed equally to this work.
‡ yehong.chen@fzu.edu.cn
§ kaixu@iphy.ac.cn
¶ hfan@iphy.ac.cn

I. MODEL AND HAMILTONIAN

A. Anisotropic quantum Rabi model

The anisotropic quantum Rabi model (AQRM) [1] generalizes the standard quantum Rabi model (QRM) by allowing the rotating and counterrotating interactions to be controlled by two independent coupling constants. The Hamiltonian reads ($\hbar = 1$)

$$\hat{H} = \omega\hat{a}^\dagger\hat{a} + \frac{\Omega}{2}\hat{\sigma}_z + g_1(\hat{a}^\dagger\hat{\sigma}_- + \hat{a}\hat{\sigma}_+) + g_2(\hat{a}^\dagger\hat{\sigma}_+ + \hat{a}\hat{\sigma}_-) + \frac{\varepsilon}{2}\hat{\sigma}_x, \tag{S1}$$

where $\hat{a}^\dagger$ ($\hat{a}$) is the creation (annihilation) operator, $\hat{\sigma}_{x,y,z}$ are the Pauli matrices, $\hat{\sigma}_\pm = (\hat{\sigma}_x \pm \mathrm{i}\hat{\sigma}_y)/2$, ω is the bosonic-mode frequency, Ω is the qubit transition frequency, g_1 and g_2 are the coupling strengths of the rotating and counterrotating terms, respectively, and ε is the qubit bias. By introducing the anisotropy ratio $\lambda = g_2/g_1$, the AQRM interpolates between the Jaynes-Cummings model (JCM) ($\lambda = 0$) and the QRM ($\lambda = 1$). For the JCM with $\varepsilon = 0$, the total excitation number is conserved:

$$\hat{N} = \hat{a}^\dagger\hat{a} + \frac{1}{2}(1 + \hat{\sigma}_z). \tag{S2}$$

For $\lambda \neq 0$ and $\varepsilon = 0$, the $U(1)$ symmetry is broken to a discrete $\mathbb{Z}_2$ parity symmetry, i.e., $[\hat{H}, \hat{\mathcal{P}}] = 0$, with the parity operator

$$\hat{\mathcal{P}} = \mathrm{e}^{\mathrm{i}\pi\hat{N}} = -(-1)^{\hat{a}^\dagger\hat{a}}\hat{\sigma}_z. \tag{S3}$$

In contrast, when $\varepsilon \neq 0$, parity symmetry is broken and the energy degeneracies are reorganized. Nevertheless, a hidden symmetry can restore level crossings at special values of ε, a feature that has attracted considerable recent interest [2–4].

The AQRM admits an alternative formulation that reveals its interpretation as a two-level system coupled to both quadratures of a bosonic mode. This becomes evident by rewriting

$$\hat{H} = \omega\hat{a}^\dagger\hat{a} + \frac{\Omega}{2}\hat{\sigma}_z + g_x(\hat{a} + \hat{a}^\dagger)\hat{\sigma}_x + \mathrm{i}g_y(\hat{a} - \hat{a}^\dagger)\hat{\sigma}_y + \frac{\varepsilon}{2}\hat{\sigma}_x, \tag{S4}$$

where $g_x = (g_1 + g_2)/2$ and $g_y = (g_1 - g_2)/2$. The model can also be mapped onto a two-dimensional electron gas with both Rashba and Dresselhaus spin-orbit couplings under a perpendicular magnetic field. Here we realize the AQRM in a circuit-QED architecture.

1. *Derivation of the effective AQRM*

Our approach builds on the method originally developed in Ref. [5]. We start from the JCM,

$$\hat{H}_0 = \frac{\omega_q}{2}\hat{\sigma}_z + \omega_r\hat{a}^\dagger\hat{a} + g_0(\hat{a}^\dagger\hat{\sigma}_- + \hat{a}\hat{\sigma}_+) \tag{S5a}$$

$$= \frac{\omega_q}{2}\hat{\sigma}_z + \omega_r\hat{a}^\dagger\hat{a} + \frac{g_0}{2}(X\hat{\sigma}_x + Y\hat{\sigma}_y), \tag{S5b}$$

where $X = (\hat{a} + \hat{a}^\dagger)$ and $Y = i(\hat{a} - \hat{a}^\dagger)$. This Hamiltonian provides an excellent description of standard circuit quantum electrodynamics (cQED) devices [6, 7]. Both the qubit frequency

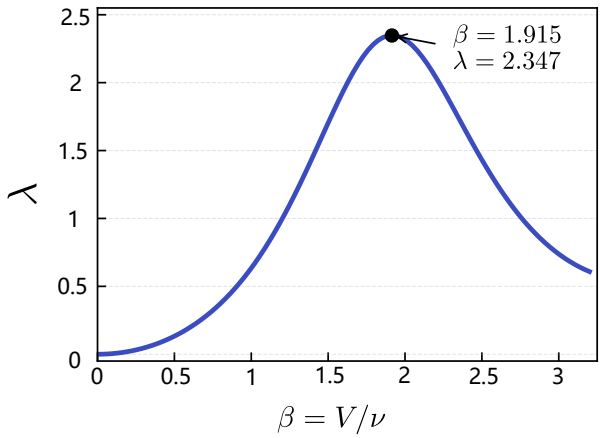

FIG. S1. Effective tunable range of λ as a function of $\beta = V/\nu$.

ω_q and the coupling strength g_0 can be finely tuned [8]. The key step in synthesizing the AQRM is to introduce a three-tone transverse field together with a longitudinal drive. The corresponding Hamiltonian in the laboratory frame is

$$\hat{H} = \frac{\omega_q}{2}\hat{\sigma}_z + \frac{A}{2}\cos\mu t\hat{\sigma}_z + \omega_r\hat{a}^\dagger\hat{a} + g_0(\hat{a}^\dagger\hat{\sigma}_- + \hat{a}\hat{\sigma}_+) + [V_0 + V\cos(\nu t)](\mathrm{e}^{\mathrm{i}\omega_0 t}\hat{\sigma}_- + \mathrm{H.c.}), \quad \text{(S6)}$$

where A and μ are the amplitude and frequency of the longitudinal field, respectively; $\{V_0, V/2\}$ are the amplitudes of the three-tone transverse field; and $\{\omega_0, \omega_0 \pm \nu\}$ are the corresponding drive frequencies. We first perform the unitary transformation

$$\hat{U}_1 = \exp\left\{i\omega_0 t(\frac{1}{2}\hat{\sigma}_z + \hat{a}^\dagger\hat{a})\right\}, \quad \text{(S7)}$$

yielding the system Hamiltonian in the rotating frame:

$$\hat{H}_I = \hat{U}\hat{H}\hat{U}^\dagger - i\hat{U}\dot{\hat{U}}^\dagger \quad \text{(S8a)}$$

$$= \frac{1}{2}(\omega_q - \omega_0 + A\cos\mu t)\hat{\sigma}_z + (\omega_r - \omega_0)\hat{a}^\dagger\hat{a} + g_0(\hat{a}^\dagger\hat{\sigma}_- + \hat{a}\hat{\sigma}_+) + [V_0 + V\cos(\nu t)]\hat{\sigma}_x. \quad \text{(S8b)}$$

The above equation can be understood in a spin-1/2 picture, by rewriting it as

$$\hat{H}_I = (\frac{g_0}{2}X + V_0 + V\cos(\nu t))\hat{\sigma}_x + \frac{g_0}{2}Y\hat{\sigma}_y + \frac{1}{2}(\omega_q - \omega_0 + A\cos\mu t)\hat{\sigma}_z + (\omega_r - \omega_0)\hat{a}^\dagger\hat{a}. \quad \text{(S9)}$$

The spin is subjected to a transverse magnetic field induced by a quantized cavity field. Since $\hat{\sigma}_y$ induces tunneling between the eigenstates of $\hat{\sigma}_x$, fast modulation of the $\hat{\sigma}_x$ term can renormalize the $\hat{\sigma}_y$ component, in analogy with the dynamical control of hopping in driven lattice systems [9–11].

Specifically, we implement a second unitary transformation

$$\hat{U}_2 = \exp\left\{\mathrm{i}\beta\sin(\nu t)\hat{\sigma}_x\right\}, \quad \text{(S10)}$$

with $\beta = V/\nu$. The system Hamiltonian in this new frame can be calculated as

$$\hat{H}_I' = \mathrm{e}^{\mathrm{i}\beta\sin\nu t\hat{\sigma}_x}[\hat{H}_I - V\cos\nu t\hat{\sigma}_x]\mathrm{e}^{-\mathrm{i}\beta\sin\nu t\hat{\sigma}_x} \tag{S11a}$$

$$= (\omega_r - \omega_0)\hat{a}^\dagger\hat{a} + \frac{1}{2}(\omega_q - \omega_0 + A\cos\mu t)\begin{bmatrix}\cos(2\beta\sin\nu t) & \mathrm{i}\sin(2\beta\sin\nu t)\\ -\mathrm{i}\sin(2\beta\sin\nu t) & -\cos(2\beta\sin\nu t)\end{bmatrix} \tag{S11b}$$

$$+ \frac{g_0}{2}(\hat{a}^\dagger\begin{bmatrix}-\mathrm{i}\sin(2\beta\sin\nu t) & 1-\cos(2\beta\sin\nu t)\\ 1+\cos(2\beta\sin\nu t) & \mathrm{i}\sin(2\beta\sin\nu t)\end{bmatrix} + \mathrm{H.c.}) + V_0\hat{\sigma}_x. \tag{S11c}$$

The qubit-frequency term becomes

$$\hat{H}_q' = \frac{1}{2}(\omega_q - \omega_0 + A\cos\mu t)[\cos(2\beta\sin\nu t)\hat{\sigma}_z - \sin(2\beta\sin\nu t)\hat{\sigma}_y], \tag{S12}$$

and the interaction term can be written as

$$\hat{H}_{\mathrm{int}}' = \frac{g_0}{2}(\hat{a} + \hat{a}^\dagger)\hat{\sigma}_x + \mathrm{i}\frac{g}{2}\cos(2\beta\sin\nu t)(\hat{a} - \hat{a}^\dagger)\hat{\sigma}_y. \tag{S13}$$

Using the Jacobi-Anger expansion

$$e^{\mathrm{i}\alpha\sin\nu t} = \sum_{n=-\infty}^{\infty} J_n(\alpha)e^{\mathrm{i}n\nu t}, \tag{S14}$$

where $J_n(\cdot)$ is the n-th Bessel function of the first kind. This gives

$$\cos(2\beta\sin\nu t) = J_0(2\beta) + 2\sum_{k=1}^{\infty} J_{2k}(2\beta)\cos 2k\nu t, \tag{S15a}$$

$$\sin(2\beta\sin\nu t) = 2\sum_{k=1}^{\infty} J_{2k-1}(2\beta)\sin(2k-1)\nu t. \tag{S15b}$$

Under the conditions $\mu = 2\nu$ and $\mu \gg A/2, g_0/2$, the Hamiltonian Eq. (S11) reduces to the AQRM Eq. (S1), where the parameters are defined as $\Omega = AJ_2(2\beta) + (\omega_q - \omega_0)J_0(2\beta)$, $\omega = \omega_r - \omega_0$, $g_1 = g_0(1 + J_0(2\beta))/2$, $g_2 = g_0(1 - J_0(2\beta))/2$ and $\varepsilon = 2V_0$. The anisotropy ratio is given by

$$\lambda = \frac{1 - J_0(2\beta)}{1 + J_0(2\beta)}, \tag{S16}$$

which has a tunable range from 0 to 2.347, as plotted in Fig. S1.

2. Duality mapping

A Pauli $\hat{\sigma}_x$ transformation maps the rotating and counterrotating channels onto each other:

$$\hat{\sigma}_x(\hat{a}^\dagger\hat{\sigma}_- + \hat{a}\hat{\sigma}_+)\hat{\sigma}_x = \hat{a}^\dagger\hat{\sigma}_+ + \hat{a}\hat{\sigma}_-, \tag{S17}$$

This follows from $\hat{\sigma}_x\hat{\sigma}_\pm\hat{\sigma}_x = \hat{\sigma}_\mp$ and $\hat{\sigma}_x\hat{\sigma}_z\hat{\sigma}_x = -\hat{\sigma}_z$, and provides an exact mapping from the $\lambda > 1$ sector to the $0 < \lambda < 1$ sector of the AQRM through

$$\hat{\sigma}_x\hat{H}(\omega, \Omega, g_1, g_2, \varepsilon)\hat{\sigma}_x = \hat{H}(\omega, -\Omega, g_1, g_2, \varepsilon). \tag{S18}$$

Experimentally, this duality allows a target AQRM with anisotropy λ to be realized by implementing its dual Hamiltonian at $1/\lambda$ with opposite qubit frequency, together with single-qubit X gates before and after the evolution.

B. Dynamics under anisotropic interactions

Here we discuss the dynamics generated by a purely anisotropic interaction,

$$\hat{H}_{\text{int}} = g_1(\hat{a}^\dagger\hat{\sigma}_- + \hat{a}\hat{\sigma}_+) + g_2(\hat{a}^\dagger\hat{\sigma}_+ + \hat{a}\hat{\sigma}_-), \tag{S19}$$

for the initial state $|\psi_0\rangle = |0, e\rangle$. In general, this evolution does not admit a simple closed-form expression. We therefore consider three limiting cases:

- When $g_1 = g$ and $g_2 = 0$, the Hamiltonian exhibits a $U(1)$ symmetry associated with conservation of the total excitation number. In this case, the state at time t is

$$|\psi\rangle = \cos gt\,|0, e\rangle - \mathrm{i}\sin gt\,|1, g\rangle\,, \tag{S20}$$

  which clearly preserves the total excitation number of $N = 1$.

- For $g_1 = g_2 = g$, the state evolves into an entangled Schrödinger cat state:

$$\begin{aligned}
|\psi\rangle =& \mathrm{e}^{-\mathrm{i}gt\hat{\sigma}_x(\hat{a}+\hat{a}^\dagger)}\frac{1}{\sqrt{2}}\,|0, +\rangle + |0, -\rangle & \text{(S21a)}\\
=& \frac{1}{\sqrt{2}}(|-\mathrm{i}gt\rangle \otimes |+\rangle + |\mathrm{i}gt\rangle \otimes |-\rangle) & \text{(S21b)}\\
=& \frac{1}{2}[(|-\mathrm{i}gt\rangle + |\mathrm{i}gt\rangle)\,|e\rangle + (|-\mathrm{i}gt\rangle - |\mathrm{i}gt\rangle)\,|g\rangle] & \text{(S21c)}\\
=& \frac{1}{2}(\mathcal{N}_+\,|\mathcal{C}^+\rangle\,|e\rangle + \mathcal{N}_-\,|\mathcal{C}^-\rangle\,|g\rangle), & \text{(S21d)}
\end{aligned}$$

  where $|-\mathrm{i}gt\rangle = \mathcal{D}(-\mathrm{i}gt)\,|0\rangle$ is a coherent state with displacement operator $\mathcal{D}(\alpha) = \mathrm{e}^{\alpha\hat{a}^\dagger - \alpha^*\hat{a}}$, and $|\mathcal{C}^\pm\rangle = (|-\mathrm{i}gt\rangle \pm |\mathrm{i}gt\rangle)/\mathcal{N}_\pm$ are photonic cat states with normalization $\mathcal{N}_\pm = \sqrt{2(1 \pm \mathrm{e}^{-2g^2t^2})}$. The total excitation number varies in time as

$$\langle\hat{N}\rangle = g^2t^2\coth(2g^2t^2) + \frac{1}{2}, \tag{S22}$$

  and the resonator photon number is $\langle\hat{a}^\dagger\hat{a}\rangle = g^2t^2\coth(2g^2t^2)$, exhibiting asymptotic growth proportional to t^2.

- When $g_1 = 0$ and $g_2 = g$, since $\hat{a}^\dagger\hat{\sigma}_+\,|0, e\rangle = \hat{a}\hat{\sigma}_-\,|0, e\rangle = 0$, the state remains in $|0, e\rangle$ with a constant total excitation number of 1.

For $0 < \lambda < 1$ and $\lambda > 1$, the total excitation number N smoothly interpolates between a constant value and quadratic growth in time. For a fixed evolution time t, N reaches its peak as a function of λ when $g_1 + g_2 = J$ is held constant. Rewriting the Hamiltonian as

$$\hat{H}_\lambda = \frac{J}{2}(\hat{H}_{\text{r}} + \hat{H}_{\text{cr}}) + \frac{J(1-\lambda)}{2(1+\lambda)}(\hat{H}_{\text{r}} - \hat{H}_{\text{cr}}). \tag{S23}$$

we define

$$F(\lambda) = \langle 0, e|\,\mathrm{e}^{\mathrm{i}\hat{H}_\lambda t}\hat{N}\mathrm{e}^{-\mathrm{i}\hat{H}_\lambda t}\,|0, e\rangle\,, \tag{S24}$$

and the corresponding derivative at $\lambda = 1$ is given by

$$F'(1) = -\mathrm{Re}\left[\int_0^1 \mathrm{d}\alpha \ \langle 0,e|\, \mathrm{e}^{\mathrm{i}\alpha\frac{Jt}{2}(\hat{H}_\mathrm{r}+\hat{H}_\mathrm{cr})}(\hat{H}_\mathrm{r}-\hat{H}_\mathrm{cr})\mathrm{e}^{\mathrm{i}(1-\alpha)\frac{Jt}{2}(\hat{H}_\mathrm{r}+\hat{H}_\mathrm{cr})}\hat{N}\mathrm{e}^{-\mathrm{i}\frac{Jt}{2}(\hat{H}_\mathrm{r}+\hat{H}_\mathrm{cr})}\,|0,e\rangle\right], \tag{S25}$$

where we have used Wilcox's formula

$$\frac{\mathrm{d}}{\mathrm{d}t}\mathrm{e}^{\hat{X}(t)} = \int_0^1 \mathrm{d}\alpha\ \mathrm{e}^{\alpha\hat{X}(t)}\frac{\mathrm{d}}{\mathrm{d}t}\hat{X}(t)\mathrm{e}^{(1-\alpha)\hat{X}(t)}. \tag{S26}$$

The left vector can be calculated in the basis $\{|+\rangle, |-\rangle\}$ as

$$\begin{aligned}
\langle\Phi| =& \langle 0,e|\, \mathrm{e}^{\mathrm{i}\alpha\frac{Jt}{2}(\hat{H}_\mathrm{r}+\hat{H}_\mathrm{cr})}(\hat{H}_\mathrm{r}-\hat{H}_\mathrm{cr})\mathrm{e}^{-\mathrm{i}\alpha\frac{Jt}{2}(\hat{H}_\mathrm{r}+\hat{H}_\mathrm{cr})} && \text{(S27a)}\\
=& \langle 0,e|\, \mathrm{e}^{\mathrm{i}\alpha\frac{Jt}{2}(\hat{H}_\mathrm{r}+\hat{H}_\mathrm{cr})}\mathrm{i}(\hat{a}-\hat{a}^\dagger)\hat{\sigma}_y\mathrm{e}^{-\mathrm{i}\alpha\frac{Jt}{2}(\hat{H}_\mathrm{r}+\hat{H}_\mathrm{cr})} && \text{(S27b)}\\
=& \frac{1}{\sqrt{2}}\begin{bmatrix}\langle 0| & \langle 0|\end{bmatrix}\begin{bmatrix}\mathcal{D}(-\mathrm{i}\alpha\frac{Jt}{2})(\hat{a}-\hat{a}^\dagger)\mathcal{D}(-\mathrm{i}\alpha\frac{Jt}{2}) & -\mathcal{D}(\mathrm{i}\alpha\frac{Jt}{2})(\hat{a}-\hat{a}^\dagger)\mathcal{D}(\mathrm{i}\alpha\frac{Jt}{2})\end{bmatrix}, && \text{(S27c)}\\
& && \text{(S27d)}
\end{aligned}$$

while the right vector becomes

$$\begin{aligned}
|\Psi\rangle =& \mathrm{e}^{\mathrm{i}\frac{Jt}{2}(\hat{H}_\mathrm{r}+\hat{H}_\mathrm{cr})}\hat{N}\mathrm{e}^{-\mathrm{i}\frac{Jt}{2}(\hat{H}_\mathrm{r}+\hat{H}_\mathrm{cr})}\,|0,e\rangle && \text{(S28a)}\\
=& \begin{bmatrix}\mathcal{D}(\mathrm{i}\frac{Jt}{2})(\hat{a}^\dagger\hat{a}+\frac{1}{2})\mathcal{D}(-\mathrm{i}\frac{Jt}{2}) & \frac{1}{2}\mathcal{D}(\mathrm{i}Jt)\\ \frac{1}{2}\mathcal{D}(-\mathrm{i}Jt) & \mathcal{D}(-\mathrm{i}\frac{Jt}{2})(\hat{a}^\dagger\hat{a}+\frac{1}{2})\mathcal{D}(\mathrm{i}\frac{Jt}{2})\end{bmatrix}\frac{1}{\sqrt{2}}\begin{bmatrix}|0\rangle\\ |0\rangle\end{bmatrix}. && \text{(S28b)}
\end{aligned}$$

The integrand in Eq. (S25) then evaluates to

$$G(\alpha) = \langle\Phi|\,\Psi\rangle = \frac{\mathrm{i}}{2}Jt[\mathrm{e}^{-\frac{1}{2}|(1-\alpha)Jt|^2} - \mathrm{e}^{-\frac{1}{2}|\alpha Jt|^2}], \tag{S29}$$

which is purely imaginary and satisfies $G(\alpha) + G(1-\alpha) = 0$, leading to $F'(1) = 0$. Thus, the total excitation number reaches an extremum at $\lambda = 1$; the numerical dynamics show that this extremum is the peak.

C. Collapses and revivals in the USC/DSC regimes

Collapses and revivals of the initial population were first predicted in the JCM regime for a coherent initial state. This phenomenon disappears with increasing g/ω but reemerges in the ultrastrong coupling (USC) and deep-strong coupling (DSC) regimes for a Fock initial state. Here we examine the corresponding behavior in the AQRM using a procedure analogous to Ref. [12].

In the unbiased AQRM the $\mathbb{Z}_2$ parity is conserved, so the dynamics is confined to two disconnected parity chains

$$\begin{aligned}
&|0,g\rangle \leftrightarrow |1,e\rangle \leftrightarrow |2,g\rangle \leftrightarrow |3,e\rangle \cdots \qquad (p=+1), && \text{(S30a)}\\
&|0,e\rangle \leftrightarrow |1,g\rangle \leftrightarrow |2,e\rangle \leftrightarrow |3,g\rangle \cdots \qquad (p=-1), && \text{(S30b)}
\end{aligned}$$

where neighboring links are generated by rotating and counter-rotating processes with generally different amplitudes. Introducing the parity basis $|p, n_b\rangle$ and the composite operator $\hat{b} = \hat{a}\hat{\sigma}_x$, the AQRM can be written as

$$\hat{H} = \omega\hat{a}^\dagger\hat{a} + \frac{\Omega}{2}\hat{\sigma}_z + g_x(\hat{a} + \hat{a}^\dagger)\hat{\sigma}_x + \mathrm{i}g_y(\hat{a} - \hat{a}^\dagger)\hat{\sigma}_y, \tag{S31a}$$

$$= \omega\hat{b}^\dagger\hat{b} - \frac{\Omega}{2}(-1)^{\hat{b}^\dagger\hat{b}}\Pi + g_x(\hat{b} + \hat{b}^\dagger) + g_y(-1)^{\hat{b}^\dagger\hat{b}}\Pi(\hat{b}^\dagger - \hat{b}), \tag{S31b}$$

which makes explicit that anisotropy introduces an additional orthogonal coupling channel (the g_y term) within each parity sector.

For a given initial state $|\psi(0)\rangle$, the revival probability can be expressed as

$$P_r(t) = \left| \sum_l |\langle\psi(0)\rangle\, \phi_l|^2\, e^{-\mathrm{i}E_l t} \right|^2, \tag{S32}$$

where $\{|\phi_l\rangle\}$ and $\{E_l\}$ are eigenstates and eigenenergies of $\hat{H}$ in the relevant parity sector.

At the isotropic point and in the degenerate case $\Omega = 0$, the Hamiltonian reduces to a displaced oscillator,

$$\hat{H}_{\mathrm{iso}} = \omega\hat{b}^\dagger\hat{b} + g_x(\hat{b} + \hat{b}^\dagger) = \omega\left(\hat{b}^\dagger + \frac{g_x}{\omega}\right)\left(\hat{b} + \frac{g_x}{\omega}\right) - \frac{g_x^2}{\omega}, \tag{S33}$$

yielding an exactly equally spaced spectrum

$$E_n = n\omega - \frac{g_x^2}{\omega}, \qquad n = 0, 1, 2, \ldots, \tag{S34}$$

and hence exact periodic revival with $T = 2\pi/\omega$. For generic anisotropy ($g_y \neq 0$), this displaced-oscillator reduction no longer applies: the orthogonal channel reshapes the dressed spacings within each parity sector, so the spectrum is no longer an elementary equally spaced ladder. Nevertheless, the AQRM remains exactly solvable in the standard sense: in each parity sector one can construct a transcendental G-function whose zeros determine the spectrum implicitly [1],

$$G_\pm(E) = 0, \tag{S35}$$

with $\pm$ labeling the two parity sectors (together with possible exceptional solutions associated with level crossings). Like the nondegenerate case of the QRM, when $\lambda \sim 1$, energy levels of AQRM deviate slightly from the equal-spaced distribution, leading to incomplete revivals of wave packets.

D. Hidden symmetry and tunneling dynamics

1. *Spectra of AQRM when $\varepsilon = 0$*

We first discuss the spectrum of the AQRM when parity symmetry is conserved, i.e., $\varepsilon = 0$. As in the standard QRM [13], the spectrum contains regular and exceptional parts. The regular spectrum is defined by the zeros of a transcendental function and can be explicitly labeled by the two eigenvalues of the parity operator. The exceptional spectrum, by contrast,

is characterized by doubly degenerate level crossings in the parameter space $(\omega, \Omega, g_1, g_2)$. These level crossings occur at energies

$$E_n = n\omega - \frac{(1+\lambda)^2 g_1^2}{2\omega}, \tag{S36}$$

with integers $n = 0, 1, 2, \cdots$. In particular, the case of $n = 0$ corresponds to the crossing between the ground state and the first excited state. This specific degeneracy arises when the parameters satisfy the analytic condition:

$$g_{1c} = \sqrt{\frac{\Omega\omega}{1-\lambda^2}}. \tag{S37}$$

Notably, such a crossing is forbidden in the isotropic QRM when $\lambda = 1$.

2. Exact solutions of AQRM

In general, the eigenvalues of the AQRM are determined by the zeros of the G-function, $G_\varepsilon(x) = 0$, where $E_n = x_n - \lambda g^2/\omega$. This function is constructed from infinite power series whose coefficients K_n satisfy a three-term recurrence relation,

$$a_n(x)K_{n+1} = b_n(x)K_n + c_n(x)K_{n-1} \tag{S38}$$

The complexity of this exact approach arises because the energy E is embedded in the coefficients a_n, b_n, c_n. Solving for the spectrum therefore requires finding the roots of a highly nonlinear transcendental function, which obscures the intuitive mechanism behind the tunneling dynamics.

For each root x_n, the corresponding exact eigenstate $|\Psi_n\rangle$ is an entangled state of the qubit and the displaced cavity field. In the original representation, it can be expressed as

$$|\Psi_n\rangle = U(\lambda,\theta)\begin{pmatrix}\phi_1(x_n)\\ \phi_2(x_n)\end{pmatrix} = U(\lambda,\theta)\sum_{m=0}^{\infty}\begin{pmatrix}L_m^+(x_n)\\ K_m^+(x_n)\end{pmatrix}|m\rangle_B \tag{S39}$$

where $|m\rangle_B$ represents the basis states in Bargmann space and $U(\lambda,\theta)$ is defined as

$$U(\lambda,\theta) = \frac{1}{\sqrt{1+\lambda}}\begin{pmatrix}1 & -\sqrt{\lambda}\\ \sqrt{\lambda} & 1\end{pmatrix} \tag{S40}$$

(Note: In this derivation, we set the phase factor $\theta = 0$, consistent with the preceding sections). The component functions $\phi_1(z)$ and $\phi_2(z)$ are defined by infinite power series:

$$\phi_1(z) = \exp\left(-\frac{\sqrt{\lambda}g}{\omega_c}z\right)\sum_{m=0}^{\infty}L_m^+\left(z+\frac{\sqrt{\lambda}g}{\omega_c}\right)^m \tag{S41}$$

$$\phi_2(z) = \exp\left(-\frac{\sqrt{\lambda}g}{\omega_c}z\right)\sum_{m=0}^{\infty}K_m^+\left(z+\frac{\sqrt{\lambda}g}{\omega_c}\right)^m \tag{S42}$$

The coefficients L_m^+ and K_m^+ are determined by

$$L_m^+ = \frac{fK_m^+ - (1-\lambda)g(m+1)K_{m+1}^+}{m\omega_c - \mathcal{E} + c} \tag{S43}$$

where $f = d + (1-\lambda)\sqrt{\lambda}g^2/\omega_c$. The coefficients K_m^+ satisfy

$$a_n(\mathcal{E})K_{n+1}^+ = b_n(\mathcal{E})K_n^+ + c_n(\mathcal{E})K_{n-1}^+ \tag{S44}$$

with $K_{-1}^+ = 0, K_0^+ = 1$. The recurrence coefficients are

$$a_n(\mathcal{E}) = 2\sqrt{\lambda} - \frac{(1-\lambda)f}{n\omega_c - \mathcal{E} + c}(n+1)g \tag{S45}$$

$$b_n(\mathcal{E}) = \frac{4\lambda g^2}{\omega_c} + n\omega_c - \mathcal{E} - c - \frac{f^* f}{n\omega_c - \mathcal{E} + c} - \frac{(1-\lambda)^2 g^2 n}{(n-1)\omega_c - \mathcal{E} + c} \tag{S46}$$

$$c_n(\mathcal{E}) = -2\sqrt{\lambda}g + \frac{(1-\lambda)gf}{(n-1)\omega_c - \mathcal{E} + c} \tag{S47}$$

The complexity of this exact approach is two-fold:

1. *Mathematical Intractability:* The energy E is not an explicit variable but is buried within the coefficients of an infinite series. Finding the roots x_n requires high-precision numerical searches for the zeros of $G_\varepsilon(x)$.

2. *Physical Obscurity:* Since $|\Psi_n\rangle$ involves an infinite summation over displaced Fock states, the intuitive mechanism of tunneling (e.g., the transition between two specific potential wells) is hidden.

This motivates the effective-Hamiltonian treatment in the following section, where a controlled approximation truncates this complexity and exposes the tunneling dynamics more directly.

3. Selective tunneling

When introducing a bias term, the isotropic QRM is promoted to the biased QRM. The bias explicitly breaks the $\mathbb{Z}_2$ parity symmetry, so the familiar parity-resolved decomposition into disconnected chains no longer applies. Remarkably, as emphasized by [3], this does *not* imply a featureless spectrum or dynamics: at special bias points $\varepsilon/\omega \in \mathbb{Z}$, the AQRM exhibits a hidden symmetry that protects level crossings and imposes additional selection rules. A direct dynamical consequence is the emergence of *selective tunneling*: preparing a wave packet localized on one displaced-oscillator branch, the time evolution can display strongly enhanced or strongly suppressed tunneling depending on whether the bias is tuned to (or away from) the hidden-symmetry condition. Operationally, this can be quantified by the branch (or target-state) overlap

$$P_{\mathrm{tun}}(t) = \left|\langle\psi_{\mathrm{target}}|e^{-iH_{\mathrm{AQRM}}t}|\psi(0)\rangle\right|^2, \tag{S48}$$

which develops a pronounced tunneling oscillation in the generic biased case, but becomes qualitatively reorganized at the hidden-symmetry points in accordance with the protected crossings and the associated selection rule [2]. In this way, the biased model provides a sharp contrast to the unbiased QRM: instead of being organized by an explicit parity conservation, the spectrum and the tunneling dynamics are reorganized by a discrete set of bias-tuned hidden-symmetry conditions.

While the biased isotropic Rabi model reveals hidden symmetry at discrete bias values, a richer structure emerges when the coupling becomes anisotropic, i.e., when the rotating and counterrotating terms have distinct strengths $g_{\rm r} \neq g_{\rm cr}$. As discussed above for the unbiased AQRM, coherent tunneling proceeds through a squeezed phase space with a deflected spin-polarization axis. When a bias is added to the anisotropic model, the hidden-symmetry condition becomes a function of both ε and λ, leading to a two-dimensional discrete set of protected level crossings. Consequently, the tunneling dynamics displays a richer form of selectivity: by tuning either the bias or the anisotropy ratio, one can switch among enhanced, suppressed, and nearly blocked tunneling. This interplay between bias-tuned and anisotropy-tuned hidden symmetries opens a route to controlling quantum tunneling in circuit-QED and trapped-ion systems, where both anisotropy and bias are experimentally accessible.

4. Approximate tunneling states

To handle the bias term $\varepsilon\hat{\sigma}_x$ and the anisotropic coupling, we apply a unitary transformation U_1 to the qubit subspace [1]:

$$U_1 = \frac{1}{\sqrt{1+\lambda}} \begin{pmatrix} 1 & -\sqrt{\lambda} \\ \sqrt{\lambda} & 1 \end{pmatrix} \tag{S49}$$

The transformed Hamiltonian $H_2 = U_1^\dagger H_1 U_1$ takes the form

$$H_2 = \begin{pmatrix} \omega a^\dagger a + \sqrt{\lambda} g_1 (a + a^\dagger) + c & (1-\lambda) g_1 a - d \\ (1-\lambda) g_1 a^\dagger - d & \omega a^\dagger a - \sqrt{\lambda} g_1 (a + a^\dagger) - c \end{pmatrix} \tag{S50}$$

where the coefficients are

$$c = \frac{1-\lambda}{1+\lambda}\frac{\Delta}{2} + \frac{\sqrt{\lambda}}{1+\lambda}\varepsilon, \quad d = \frac{\sqrt{\lambda}}{1+\lambda}\Delta - \frac{1-\lambda}{1+\lambda}\frac{\varepsilon}{2} \tag{S51}$$

To eliminate the longitudinal coupling terms $\sqrt{\lambda} g_1 (a + a^\dagger)\hat{\sigma}_z$, we introduce a conditional displacement operator,

$$U_2 = \exp\left[-\frac{\sqrt{\lambda} g_1}{\omega} \hat{\sigma}_z (a^\dagger - a) \right] \tag{S52}$$

This operator maps the system into the *displaced oscillator basis* $|n_\pm, \pm\rangle$, where the cavity field equilibrium depends on the qubit state.

The final Hamiltonian $H_3 = U_2^\dagger H_2 U_2$ is

$$H_3 = \omega a^\dagger a - \frac{\lambda g_1^2}{\omega} + c\hat{\sigma}_z + \hat{\sigma}_+ (\tilde{g} a - x) e^{k(a^\dagger - a)} + \hat{\sigma}_- (\tilde{g} a^\dagger + y) e^{-k(a^\dagger - a)} \tag{S53}$$

with $\tilde{g} = (1-\lambda) g_1$, $k = 2\sqrt{\lambda} g_1/\omega$, and parameters $x = (1-\lambda)\sqrt{\lambda} g_1^2/\omega + d, y = (1-\lambda)\sqrt{\lambda} g_1^2/\omega - d$. The exponential terms $e^{\pm k(a^\dagger - a)}$ introduce nonlinearities that couple all photon-number states.

In the limit $k \ll 1$, we perform a first-order expansion of the exponential displacement operators, $e^{\pm k(a^\dagger - a)} \approx 1 + k(a^\dagger - a)$. The system reduces to an analytical effective Jaynes-Cummings model with bias terms:

$$H_3 \approx \omega a^\dagger a + c\hat{\sigma}_z + (\tilde{g} + kx)(a\hat{\sigma}_+ + a^\dagger\hat{\sigma}_-) + (y + k\tilde{g}a^\dagger a)\hat{\sigma}_x. \tag{S54}$$

This approximation remains valid for small anisotropy and weak to moderate coupling, providing a clear intuitive picture of the underlying dynamics.

In the displaced oscillator basis, the $\hat{\sigma}_\pm$ operators act as tunneling operators between the two spatially separated potential wells. The constant term $(y + k\tilde{g}a^\dagger a)\hat{\sigma}_x$ drives direct tunneling that preserves photon number, whereas the interaction term $(\tilde{g} + kx)(a\hat{\sigma}_+ + a^\dagger\hat{\sigma}_-)$ enables photon-assisted tunneling that changes photon number. The coherent oscillations observed in our simulations directly reflect these tunneling processes at the hidden-symmetry points.

Tunneling in the biased AQRM is selective. Unlike ordinary QRM oscillations, it occurs predominantly when the bias ε satisfies the resonance condition. In the reduced model in Eq. (S54), this condition is

$$\varepsilon = \frac{1+\lambda}{2\sqrt{\lambda}} n\omega - \frac{1-\lambda}{2\sqrt{\lambda}}\Delta, \quad n = 0, 1, 2, \ldots \tag{S55}$$

At these values, the system exhibits hidden symmetry, leading to level crossings (Juddian points) in the energy spectrum.

Under the resonance condition, the tunneling occurs between the correlated states:

- For $n = 0$ ($c = 0$): $|0_+, +\rangle \leftrightarrow |0_-, -\rangle$,
- For $n = 1$ ($c = 0.5\omega$): $|0_+, +\rangle \leftrightarrow |1_-, -\rangle$,

where

$$|0_+, +\rangle = |-\frac{\sqrt{\lambda}g_1}{\omega}\rangle \otimes \left(|e\rangle + \sqrt{\lambda}\,|g\rangle\right), \tag{S56}$$

$$|0_-, -\rangle = |\frac{\sqrt{\lambda}g_1}{\omega}\rangle \otimes \left(-\sqrt{\lambda}\,|e\rangle + |g\rangle\right), \tag{S57}$$

$$|1_-, -\rangle = D\left(\frac{\sqrt{\lambda}g_1}{\omega}\right)|1\rangle \otimes \left(-\sqrt{\lambda}\,|e\rangle + |g\rangle\right). \tag{S58}$$

The corresponding quasi-eigenenergies are split by the tunneling matrix element, which determines the frequency of the probability oscillations observed in numerical simulations.

Because the analytical derivation above is primarily controlled in the weak-coupling regime ($g \leq 0.2\omega$), the parameters obtained from the simplified model cannot be applied directly to the experimental strong-coupling setting, where clear tunneling dynamics are easier to resolve. We therefore use a numerical approach to identify optimal parameters for realizing tunneling dynamics in the strong-coupling regime ($g \sim \omega$).

We assume that the low-energy tunneling processes are predominantly governed by a few-level subspace spanned by the displaced oscillator states $|0_+, +\rangle$, $|0_-, -\rangle$, and $|1_-, -\rangle$. We then simulate the tunneling dynamics under strong coupling. First, we plot the first ten energy levels as a function of the normalized bias parameter:

$$\varepsilon = k\frac{2\sqrt{\lambda}}{1+\lambda}\omega, \tag{S59}$$

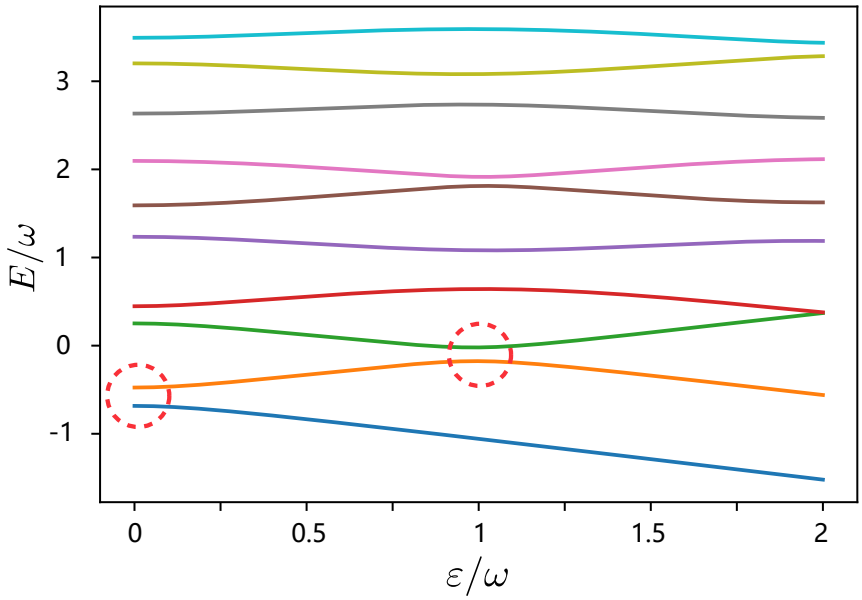

FIG. S2. Energy levels of the biased AQRM. The red dashed circles mark the tunneling processes. The parameters are $g_1 = \omega$, $\Delta = 0.1\omega$, and $\lambda = 0.5$.

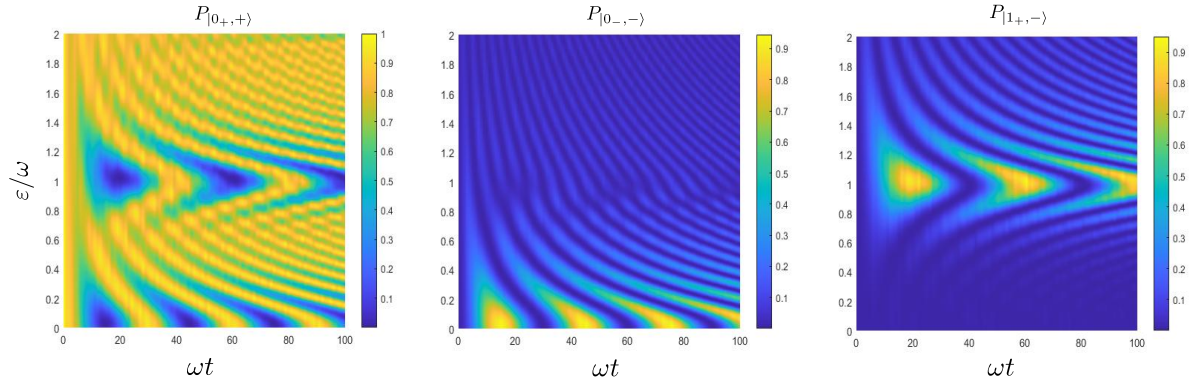

FIG. S3. Tunneling dynamics of the biased AQRM from the initial state $|0_+, +\rangle$. The population in the state (left) $|0_+, +\rangle$, (center) $|0_-, -\rangle$ and (right) $|1_-, -\rangle$. The parameters are $g = \omega$, $\Delta = 0.1\omega$, and $\lambda = 0.5$.

with integer k.

The spectrum reveals pronounced avoided level crossings at $n = 0$ and $n = 1$, indicating the formation of a nearly closed dynamical subspace at these resonance points (see Fig. S2).

To verify this assumption, we calculate the overlap (fidelity) between the three lowest eigenstates and the basis states $|0_+, +\rangle$, $|0_-, -\rangle$, and $|1_-, -\rangle$. The results confirm that these displaced states are the dominant components of the low-energy manifold during tunneling. Finally, we perform a parameter scan across different values of the normalized parameter $\bar{\varepsilon}$ to characterize the tunneling dynamics (see Fig. S3), providing a robust numerical guide for experimental observation in the strong coupling regime [3].

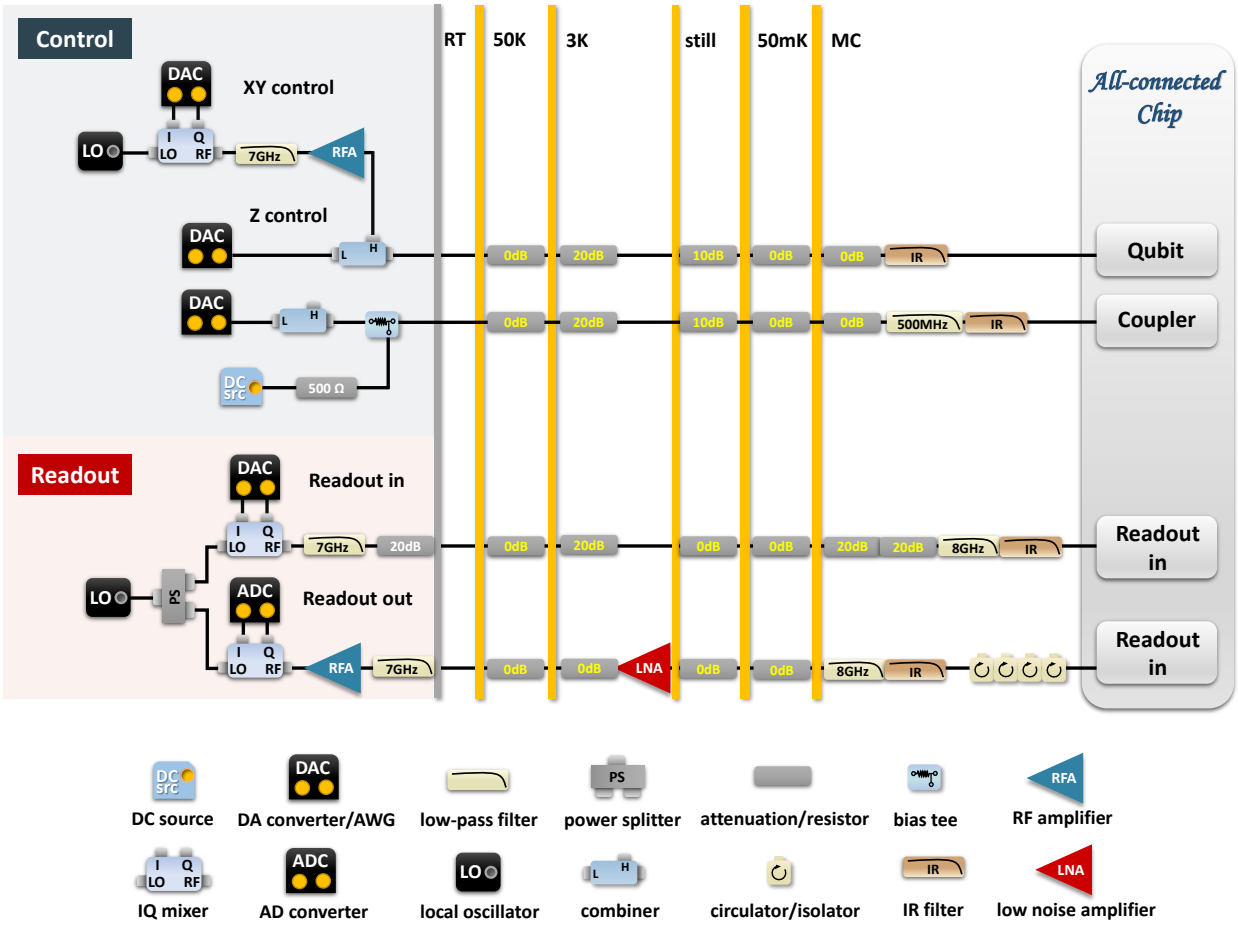

FIG. S4. **Schematic diagram of the experimental system and wiring information**

II. EXPERIMENTAL SETUP

A. Wiring layout

Figure S4 shows the wiring layout used for room-temperature and cryogenic operations. From top to bottom, the lines correspond to XY control, Z control (including fast bias and DC sources), and qubit readout (input and output) channels. Horizontally, the diagram shows the cooling stages from room temperature to 12 mK in a BlueFors XLD-1000 dilution refrigerator. Appropriate attenuation is implemented on the coaxial lines to suppress thermal noise [14].

At room temperature, the high-frequency XY signals and low-frequency Z biases (fast Z) are combined and sent to the qubits for state excitation and frequency modulation, respectively. The XY signals are generated by IQ mixers, which mix local-oscillator (LO) signals from microwave sources with IQ waveforms from arbitrary waveform generators (AWGs). To deliver the strong transverse drive used in this experiment, an additional RF amplifier (RFA) is inserted into the XY control line at room temperature. On the coupler line, only the low-frequency Z bias is delivered. To extend the available bias range and reduce distortion of fast-Z pulses, the DC source is combined with the low-frequency Z bias through bias tees before reaching the coupler.

Similarly, the readout signal is generated by mixing the AWG waveform with the LO signal through an IQ mixer. The signal collected from the readout output line is amplified by a low-noise amplifier (LNA) and a room-temperature RF amplifier (RFA). Before digitization, the RF signal is converted to an intermediate frequency through down-conversion and then sampled by analog-to-digital converters (ADCs).

B. Device performance

The experiment uses one frequency-tunable transmon qubit as the system qubit Q, a central bus resonator R, a tunable coupler C for controlling the effective qubit-resonator interaction, and an ancillary transmon qubit Q_a coupled to the resonator for photon-number-resolved resonator readout. The relevant coherence and readout characteristics of Q, Q_a, and R are summarized in Table S1. These quantities are measured at the operating points used for the AQRM experiments unless stated otherwise.

TABLE S1. **Device coherence and readout characteristics.** The symbols Q, Q_a, and R denote the system qubit, ancilla qubit, and bus resonator, respectively. T_1, T_2^*, and T_2^{SE} are the energy relaxation time, Ramsey dephasing time, and echo dephasing time, respectively.

Parameter	Q	Q_a	R
Operating frequency, $\omega_{10}/2\pi$ (GHz)	4.420	4.454	3.966
Anharmonicity, $\alpha/2\pi$ (MHz)	-370	-204	–
Relaxation time, T_1 (μs)	43.6	48.2	28.0
Ramsey dephasing time, T_2^* (μs)	10.3	13.5	–
Echo dephasing time, T_2^{SE} (μs)	20.9	23.1	–
Readout fidelity of $\|g\rangle$, F_g (%)	96.83	97.60	–
Readout fidelity of $\|e\rangle$, F_e (%)	93.80	93.73	–

For the experiments reported in the main text, the system qubit is operated in a regime where its anharmonicity suppresses leakage to higher transmon levels and supports the effective two-level description used in the AQRM Hamiltonian. The coherence times of the qubits and the resonator lifetime are longer than the relevant pulse sequences used for collapse-revival measurements, adiabatic eigenstate preparation, and tunneling oscillations, but still set the dominant decoherence limits in the experiment.

III. EXPERIMENTAL CONTROL AND CALIBRATION

A. Tunable coupler between qubit and resonator

1. *Circuit Hamiltonian*

We consider a system in which the qubit and the resonator are coupled to a tunable coupler. The equivalent circuit is shown in Supplementary Fig. S5. The resonator is modeled as an effective LC circuit. The circuit parameters satisfy the condition $C_q, C_c, C_r \gg C_{qc}, C_{rc} \gg C_{qr}$, where C_{qc} (C_{rc}) is the coupling capacitance between the qubit (resonator) and the coupler, and C_{qr} is the direct capacitance between the qubit and the resonator.

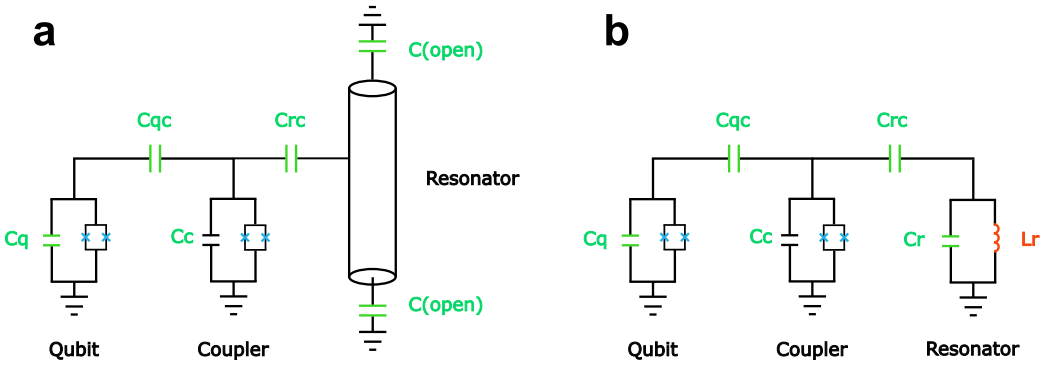

FIG. S5. **a**, Equivalent circuit model for a qubit and a resonator coupled to a tunable coupler. **b**, Effective LC-circuit representation of the resonator. The effective capacitance and inductance depend on the respective coupling positions.

The system Lagrangian is composed of kinetic (T) and potential (U) energy terms, expressed using node fluxes φ_q, φ_r, and φ_c. The kinetic energy is

$$\begin{aligned} T = &\frac{1}{2}\left[C_q\dot{\varphi_q}^2 + C_r\dot{\varphi_r}^2 + C_c\dot{\varphi_c}^2\right] \\ &+ \frac{1}{2}\left[C_{qc}\left(\dot{\varphi}_q - \dot{\varphi}_c\right)^2 + C_{rc}\left(\dot{\varphi}_r - \dot{\varphi}_c\right)^2 + C_{qr}\left(\dot{\varphi}_q - \dot{\varphi}_r\right)^2\right]. \end{aligned} \tag{S60}$$

The kinetic energy can be expressed in compact form as $T = \frac{1}{2}\dot{\boldsymbol{\varphi}}^\top C\dot{\boldsymbol{\varphi}}$, where $\boldsymbol{\varphi} = [\varphi_q, \varphi_r, \varphi_c]^\top$ and C is the 3×3 capacitance matrix

$$C = \begin{bmatrix} C_q + C_{qr} + C_{qc} & -C_{qr} & -C_{qc} \\ -C_{qr} & C_r + C_{qr} + C_{rc} & -C_{rc} \\ -C_{qc} & -C_{rc} & C_c + C_{qc} + C_{rc} \end{bmatrix}. \tag{S61}$$

Under the condition $C_q, C_c, C_r \gg C_{qc}, C_{rc} \gg C_{qr}$, the inverse capacitance matrix is approximated as

$$C^{-1} \approx \begin{bmatrix} \frac{1}{C_q} & \frac{C_{qc}C_{rc}+C_cC_{qr}}{C_qC_rC_c} & \frac{C_{qc}}{C_qC_c} \\ \frac{C_{qc}C_{rc}+C_cC_{qr}}{C_qC_rC_c} & \frac{1}{C_r} & \frac{C_{rc}}{C_rC_c} \\ \frac{C_{qc}}{C_qC_c} & \frac{C_{rc}}{C_rC_c} & \frac{1}{C_c} \end{bmatrix}. \tag{S62}$$

The conjugate charge vector is $\boldsymbol{q} = C\dot{\boldsymbol{\varphi}}$, and the classical Hamiltonian is

$$H = \frac{1}{2}\boldsymbol{q}^\top C^{-1}\boldsymbol{q} + U. \tag{S63}$$

Here, the potential energy U includes the Josephson energies of the qubit and coupler and the inductive energy of the resonator:

$$U = E_{J_q}\left[1 - \cos\left(\frac{2\pi}{\Phi_0}\varphi_q\right)\right] + E_{J_c}\left[1 - \cos\left(\frac{2\pi}{\Phi_0}\varphi_c\right)\right] + \frac{{\varphi_r}^2}{2L_r}, \tag{S64}$$

where E_{J_q} (E_{J_c}) is the Josephson energy of the qubit (coupler), and $\Phi_0 = h/(2e)$ is the flux quantum. Quantizing the system, we promote $\boldsymbol{q}$ and $\boldsymbol{\varphi}$ to operators satisfying $[\hat{\varphi}_\lambda, \hat{q}_{\lambda'}] = i\hbar\delta_{\lambda\lambda'}$. The quantized Hamiltonian is

$$\begin{aligned} \hat{H} =& 4E_{c_q}\left(\hat{n_q}\right)^2 - E_{J_q}\cos\left(\frac{2\pi}{\Phi_0}\hat{\varphi}_q\right) + 4E_{c_c}\left(\hat{n_c}\right)^2 - E_{J_c}\cos\left(\frac{2\pi}{\Phi_0}\hat{\varphi}_c\right) + 4E_{c_r}\left(\hat{n_r}\right)^2 + \frac{{\hat{\varphi}_r}^2}{2L_r} \\ &+ 8\frac{C_{qc}}{\sqrt{C_qC_c}}\sqrt{E_{c_q}E_{c_c}}\left(\hat{n_q}\hat{n_c}\right) + 8\frac{C_{rc}}{\sqrt{C_rC_c}}\sqrt{E_{c_r}E_{c_c}}\left(\hat{n_r}\hat{n_c}\right) \\ &+ 8\left(\frac{C_{qc}C_{rc}+C_cC_{qr}}{C_c\sqrt{C_qC_r}}\right)\sqrt{E_{c_q}E_{c_r}}\left(\hat{n_q}\hat{n_r}\right), \end{aligned} \tag{S65}$$

where $\hat{n}_\lambda = \hat{q}_\lambda/(2e)$ is the Cooper-pair number operator, and $E_{c_\lambda} = e^2/(2C_\lambda)$ is the charging energy for $\lambda = q, c$.

In the transmon regime ($E_{J_\lambda}/E_{c_\lambda} \gg 1$), the qubits and resonator behave as weakly anharmonic oscillators. We approximate the system as coupled Duffing oscillators ($\hbar = 1$):

$$\hat{H} = \hat{H}_q + \hat{H}_r + \hat{H}_c + \hat{H}_{qc} + \hat{H}_{rc} + \hat{H}_{qr}, \tag{S66}$$

where the individual mode Hamiltonians are

$$\hat{H}_\lambda = \omega_\lambda\hat{b}_\lambda^\dagger\hat{b}_\lambda + \frac{\alpha_\lambda}{2}\hat{b}_\lambda^\dagger\hat{b}_\lambda^\dagger\hat{b}_\lambda\hat{b}_\lambda, \quad \lambda = q, r, c, \tag{S67}$$

with anharmonicities

$$\alpha_\lambda = -E_{c_\lambda}, \quad \lambda = q, c. \tag{S68}$$

The interaction terms are

$$\hat{H}_{jc} = g_{jc}\left(\hat{b}_j^\dagger\hat{b}_c + \hat{b}_j\hat{b}_c^\dagger - \hat{b}_j^\dagger\hat{b}_c^\dagger - \hat{b}_j\hat{b}_c\right), \quad j = q, r, \tag{S69}$$

$$\hat{H}_{qr} = g_{qr}\left(\hat{b}_q^\dagger\hat{b}_r + \hat{b}_q\hat{b}_r^\dagger - \hat{b}_q^\dagger\hat{b}_r^\dagger - \hat{b}_q\hat{b}_r\right), \tag{S70}$$

with coupling strengths

$$g_{qc} = \frac{1}{2}\frac{C_{qc}}{\sqrt{C_q C_c}}\sqrt{\omega_q \omega_c}, \tag{S71}$$

$$g_{rc} = \frac{1}{2}\frac{C_{rc}}{\sqrt{C_r C_c}}\sqrt{\omega_r \omega_c}, \tag{S72}$$

$$g_{qr} = \frac{1}{2}\frac{C_{qc}C_{rc} + C_{qr}C_c}{\sqrt{C_q C_r C_c}}\sqrt{\omega_q \omega_r} = \frac{1}{2}(1+\eta)\frac{C_{qr}}{\sqrt{C_q C_r}}\sqrt{\omega_q \omega_r}, \tag{S73}$$

where

$$\eta = \frac{C_{qc}C_{rc}}{C_{qr}C_c}. \tag{S74}$$

To eliminate the qubit-coupler and resonator-coupler interactions and obtain an effective qubit-resonator coupling, we apply the Schrieffer-Wolff transformation

$$\hat{U} = \exp\left\{\sum_{j=q,r}\left[\frac{g_{jc}}{\Delta_{jc}}\left(\hat{b}_j^\dagger \hat{b}_c - \hat{b}_j \hat{b}_c^\dagger\right) - \frac{g_{jc}}{\hat{\sigma}_{jc}}\left(\hat{b}_j^\dagger \hat{b}_c^\dagger - \hat{b}_j \hat{b}_c\right)\right]\right\}, \tag{S75}$$

where

$$\Delta_{jc} = \omega_j - \omega_c, \quad \hat{\sigma}_{jc} = \omega_j + \omega_c. \tag{S76}$$

The transformed Hamiltonian is

$$\hat{\tilde{H}} = \hat{U}\hat{H}\hat{U}^\dagger = \widetilde{\omega_q}\hat{b}_q^\dagger \hat{b}_q + \frac{\widetilde{\alpha_q}}{2}\hat{b}_q^\dagger \hat{b}_q^\dagger \hat{b}_q \hat{b}_q + \widetilde{\omega_r}\hat{b}_r^\dagger \hat{b}_r + \widetilde{g}_{qr}\left(\hat{b}_q^\dagger \hat{b}_r + \hat{b}_q \hat{b}_r^\dagger\right), \tag{S77}$$

with

$$\widetilde{\omega_q} \approx \omega_q + g_{qc}^2\left(\frac{1}{\Delta_{qc}} - \frac{1}{\hat{\sigma}_{qc}}\right), \widetilde{\alpha_q} \approx \alpha_q, \tag{S78}$$

$$\widetilde{\omega_r} \approx \omega_r + g_{rc}^2\left(\frac{1}{\Delta_{rc}} - \frac{1}{\hat{\sigma}_{rc}}\right), \tag{S79}$$

$$\widetilde{g}_{qr} = \frac{g_{qc}g_{rc}}{2}\left(\frac{1}{\Delta_{qc}} + \frac{1}{\Delta_{rc}} - \frac{1}{\hat{\sigma}_{qc}} - \frac{1}{\hat{\sigma}_{rc}}\right) + g_{qr}. \tag{S80}$$

2. Tunable coupling

The effective qubit-resonator coupling is controlled in situ by tuning the coupler frequency with a flux-bias pulse. Experimentally, we calibrate the mapping from the coupler control amplitude to the effective coupling strength g_0 before implementing the synthesized AQRM. The calibration uses the coherent exchange between the system qubit and the resonator near resonance: the qubit is prepared in $|e\rangle$ while the resonator is initialized close to vacuum, the coupler is biased to a selected operating point, and the resulting vacuum-Rabi oscillation is measured as a function of interaction time. Fitting the oscillation frequency yields the corresponding value of g_0.

The measured dependence g_0 versus the bias is then used to determine the operating points for the data shown in the main text. In the present experiment, the coupling $g_0/2\pi$ can be tuned from -10 to 0 MHz, with the largest coupling used for the strongest-interaction

data. For each target value of g_0, the coupler pulse amplitude and the associated frequency shifts of the qubit and resonator are calibrated and incorporated into the rotating-frame settings used for state preparation and tomography. The calibration workflow and inverse conversion are summarized in Fig. S6.

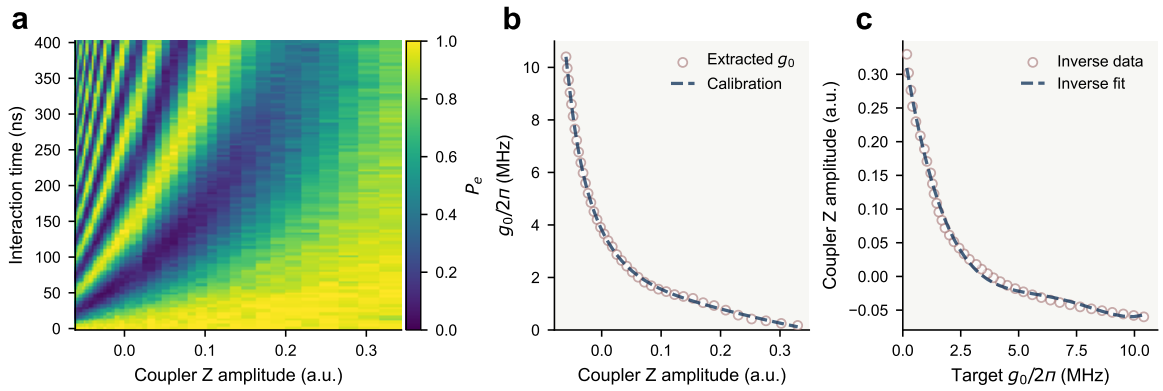

FIG. S6. **Calibration of the tunable qubit-resonator coupling.** **a**, Raw qubit-resonator exchange oscillations measured as a function of interaction time and coupler Z-pulse amplitude. **b**, Extracted effective coupling strength $g_0/2\pi$ and smooth calibration curve versus coupler Z-pulse amplitude. **c**, Inverse calibration used to convert a target coupling strength g_0 into the coupler Z-pulse amplitude for adiabatic ramps.

B. Calibration of synthesized AQRM

1. *Calibration of control fields*

The synthesized AQRM requires calibrated transverse qubit drives and longitudinal frequency modulation. The transverse terms are generated by microwave tones applied through the qubit XY line, including the carrier and the sideband tones used in the difference-frequency implementation. For each relevant tone, we calibrate the qubit response by measuring vacuum Rabi oscillations as a function of the applied microwave amplitude. The extracted response curve converts the programmed XY amplitude to the transverse drive strength used in the effective Hamiltonian.

The longitudinal modulation is applied through the qubit Z line. Because the modulation amplitude used in the experiment is small compared with the full tunable range of the qubit, the local frequency response is well approximated by a linear dependence on the Z-pulse amplitude. The measured frequency shift is therefore fitted with a first-order calibration curve and used to set the longitudinal modulation amplitude. The corresponding transverse and longitudinal calibrations are shown in Fig. S7.

2. *Displacement operators and resonator frequency*

Resonator displacements used for tomography, resonator-frequency calibration, and tunneling-state preparation are calibrated by measuring the photon number generated by

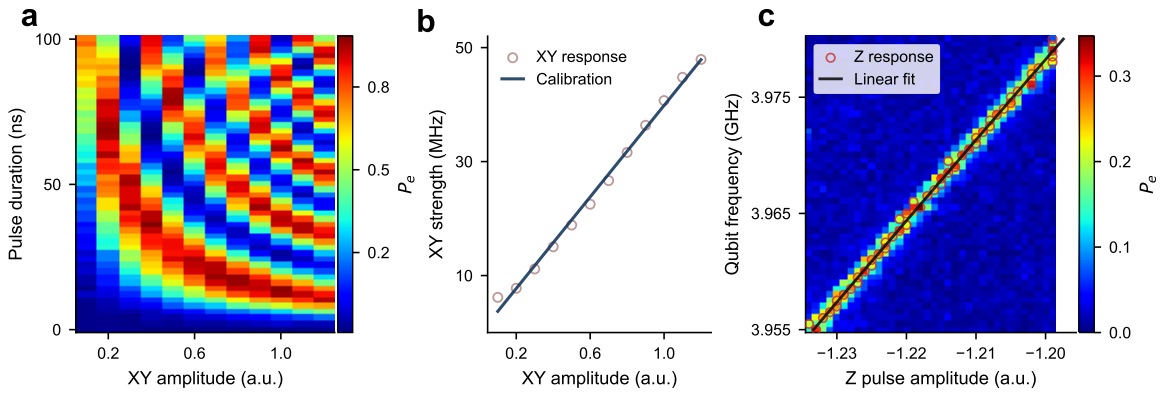

FIG. S7. **Calibration of qubit control fields.** **a**, Raw transverse Rabi response measured as a function of XY amplitude and pulse duration. **b**, Extracted transverse response calibration, which converts the applied XY amplitude to the effective transverse drive strength. **c**, Longitudinal Z response obtained by measuring the qubit frequency shift versus Z-pulse amplitude. Over the small modulation range used in the experiment, the longitudinal response is well approximated by a linear calibration.

resonant microwave pulses. For this calibration, the resonator pulse duration is fixed while its amplitude is varied. After each pulse, the photon-number distribution P_n is extracted using the photon-number-resolved readout described above, and the mean photon number is calculated as

$$\langle n \rangle = \sum_n n P_n. \tag{S81}$$

For a resonant displacement of the vacuum state, the prepared state is a coherent state $D(\alpha)\,|0\rangle$ and satisfies

$$|\alpha| = \sqrt{\langle n \rangle}. \tag{S82}$$

This provides the calibration curve between the applied pulse amplitude and the displacement amplitude $|\alpha|$. The phase of the resonator drive sets the phase of α, while the calibrated amplitude determines the displacement radius used in the tomography and state-preparation protocols. The raw readout response and the resulting displacement-amplitude calibration are shown in Fig. S8.

The resonator frequency is calibrated using a phase-to-displacement sequence. Starting from the vacuum, we apply a calibrated displacement $D(\alpha)$, let the resonator evolve for a delay time τ in the frame of a trial drive frequency ω_d, and then apply the opposite displacement $D(-\alpha)$. For a detuning $\Delta_r = \omega_r - \omega_d$, the coherent state evolves as

$$|\alpha\rangle \to |\alpha e^{-i\Delta_r \tau}\rangle\,, \qquad |\psi_f\rangle \simeq |\alpha(e^{-i\Delta_r \tau} - 1)\rangle\,, \tag{S83}$$

up to an overall phase. The residual photon number after the second displacement is therefore

$$\langle n_f \rangle = |\alpha|^2 \left|e^{-i\Delta_r \tau} - 1\right|^2 \simeq |\alpha|^2 (\Delta_r \tau)^2, \tag{S84}$$

for $|\Delta_r \tau| \ll 1$. The residual population is minimized when the trial drive frequency matches the resonator frequency. Experimentally, this residual resonator population is measured using the photon-number-resolved readout described above. The phase-to-displacement calibration data and schematic sequence are shown in Fig. S9.

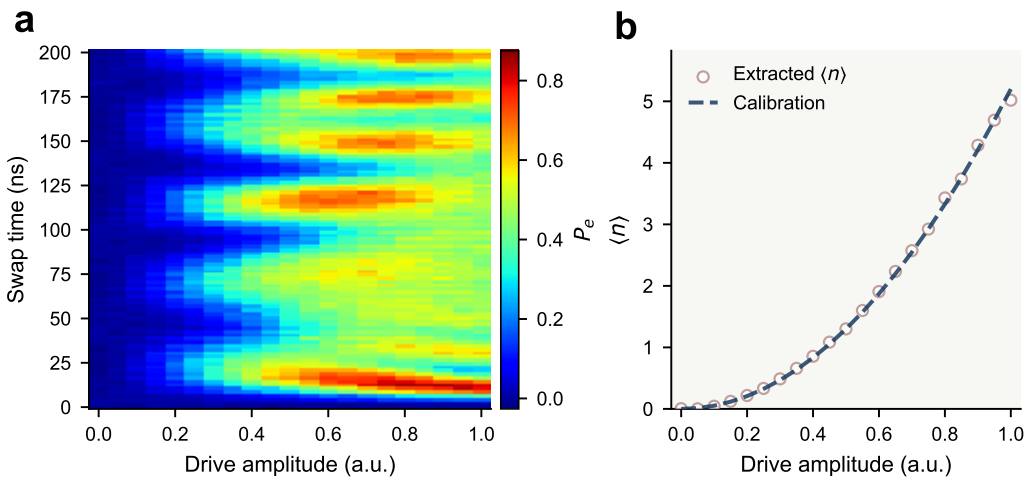

FIG. S8. **Resonator drive calibration.** **a**, Photon-number-resolved readout response measured after resonator displacement pulses with different drive amplitudes. **b**, Extracted mean photon number $\langle n \rangle$ and calibration curve versus resonator drive amplitude. For a resonant displacement of the vacuum state, the displacement amplitude is calibrated using $|\alpha| = \sqrt{\langle n \rangle}$, giving the conversion between the applied resonator pulse amplitude and the phase-space displacement used in tomography and state preparation.

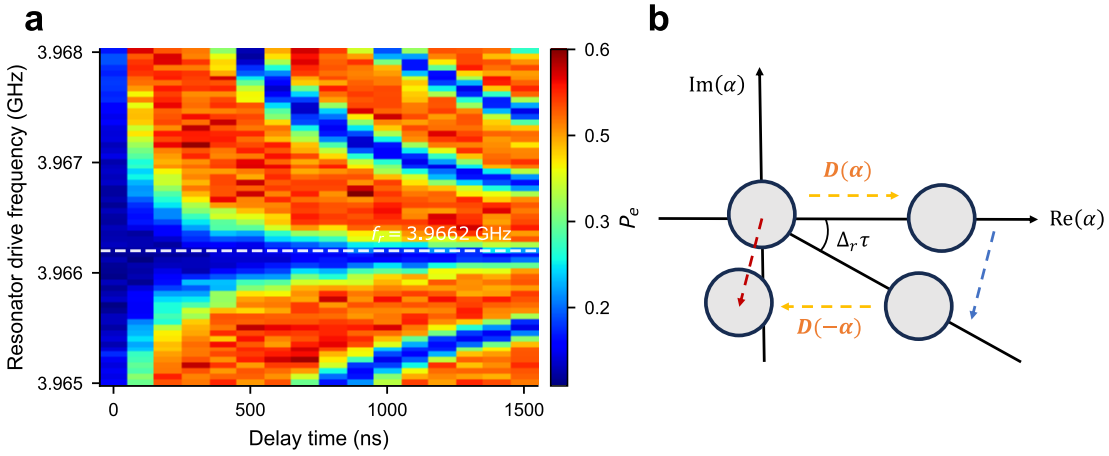

FIG. S9. **Calibration of the resonator frequency.** **a**, Phase-to-displacement calibration data measured as a function of delay time and resonator drive frequency. The residual resonator population is minimized when the drive frequency matches the resonator frequency, and the dashed line marks the calibrated value $f_r = \omega_r/2\pi = 3.9662$ GHz. **b**, Schematic of the calibration protocol: a coherent displacement is prepared, allowed to accumulate detuning-dependent phase, and then displaced back toward the vacuum.

3. Frame transformations

The synthesized AQRM is implemented from the tunable Jaynes-Cummings interaction between the system qubit and the resonator. The calibrated coupler pulse sets the bare exchange rate g_0, while the qubit control fields provide the longitudinal modulation, the carrier

tone, and the transverse sideband tones used in the effective-Hamiltonian construction. In the rotating frame of the carrier, these controls determine the effective resonator frequency ω, qubit frequency Ω, rotating and counterrotating coupling strengths g_1 and g_2, and bias ε defined in Eq. (S1).

The first frame transformation introduced in the derivation corresponds to the qubit-resonator rotating frame. It is not implemented as an additional physical gate. Instead, the accumulated phase is tracked in software and absorbed into the phase references of subsequent qubit XY pulses, resonator displacements, and tomography rotations. The second transformation,

$$\hat{U}_2(t) = \exp\left[i\beta \sin(\nu t)\hat{\sigma}_x\right], \tag{S85}$$

is implemented as a parameterized rotation around the qubit x axis. With the convention

$$X_\theta = \exp\left(-i\frac{\theta}{2}\hat{\sigma}_x\right), \tag{S86}$$

we write

$$\hat{U}_2(t) = X_{\theta_2(t)}, \qquad \theta_2(t) = -2\beta \sin(\nu t), \tag{S87}$$

up to the sign convention of the microwave drive phase.

Experimentally, the required single-qubit rotations are synthesized from calibrated $X_{\pi/2}$ pulses and virtual Z gates [15]. The decomposition

$$X_\theta = Z_{-\pi/2} X_{\pi/2} Z_{\pi-\theta} X_{\pi/2} Z_{-\pi/2} \tag{S88}$$

uses only two finite-duration microwave pulses; the Z rotations are implemented virtually by phase updates. More generally, a rotation in the equatorial plane can be written as

$$R_\phi(\theta) = \exp\left[-i\frac{\theta}{2}\left(\cos\phi\,\hat{\sigma}_x + \sin\phi\,\hat{\sigma}_y\right)\right] = Z_\phi X_\theta Z_{-\phi}. \tag{S89}$$

In particular, $R_y(\theta) = R_{\pi/2}(\theta)$, which is the parameterized single-qubit rotation used for the tunneling-state initialization below.

Figure S10 shows a dynamical check of the physical frame transformations. Applying the two single-qubit operations before and after the transformed-frame evolution changes the observed population dynamics in agreement with the numerical prediction, whereas omitting them gives a distinct control trajectory.

4. Photon-number-resolved resonator readout

The resonator photon-number distribution is measured with an ancillary qubit using resonant qubit-resonator swaps [16]. After the target evolution or calibration pulse, the resonator drive is switched off and the ancilla qubit Q_a, initially prepared in $|g\rangle$, is tuned into resonance with the resonator for a variable interaction time τ. The ancilla is then returned to its idle frequency for projective readout. The resulting photon-number-dependent vacuum-Rabi oscillation is fitted to

$$P_e(\tau) = \frac{1}{2}\left[1 - P_g(0)\sum_{n=0}^{n_{\max}} P_n e^{-\kappa_n \tau}\cos\left(2\sqrt{n}\,g_a\tau\right)\right], \tag{S90}$$

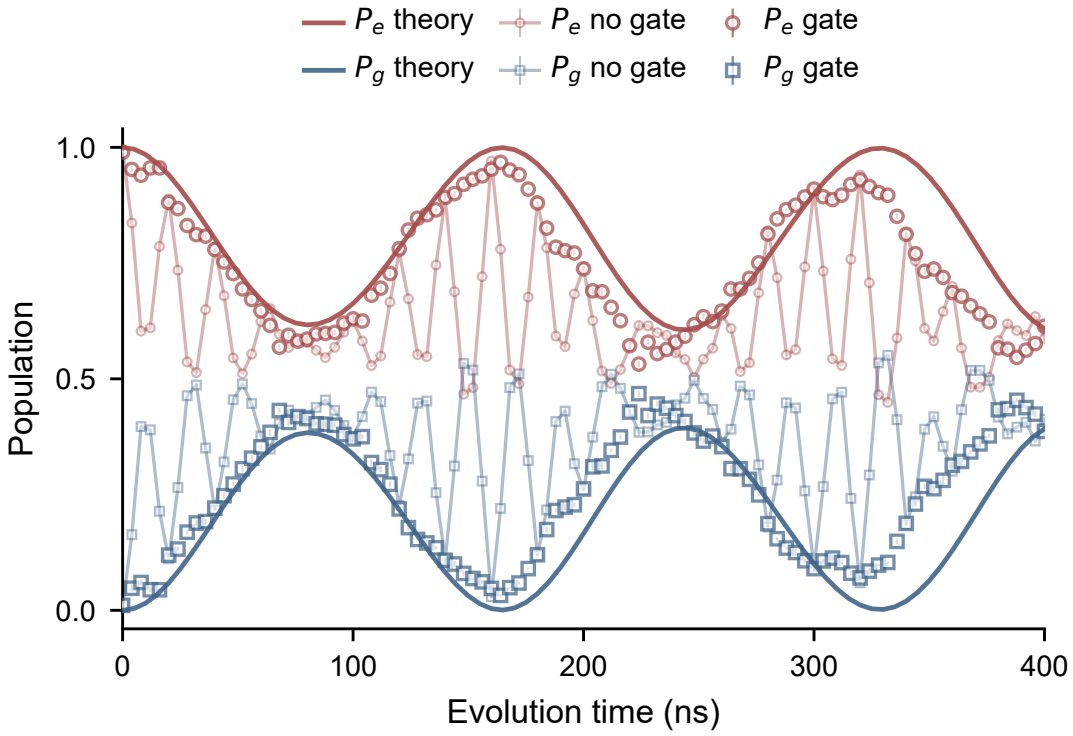

FIG. S10. **Dynamical effect of the physical frame transformations.** Measured qubit-state populations during anisotropic Rabi dynamics with and without the two physical single-qubit operations used to implement the transformed-frame evolution. The gate data are shown as open markers with error bars, while the no-gate control data are shown as lighter marker lines to emphasize the faster oscillatory component. Solid curves show the numerical prediction for the transformed-frame dynamics. Error bars denote the standard error of the mean over ten repeated measurements.

where $P_g(0)$ is the initial ground-state probability of the ancilla, $P_n = \rho_{nn}$ is the resonator photon-number distribution, $n_{\max}$ is the fitting cutoff, κ_n is an empirical decay rate for the n-photon oscillation, and g_a is the resonant ancilla-resonator coupling. In the experiment, $g_a/2\pi = 11$ MHz. The extracted distribution gives the mean photon number $\langle n \rangle = \sum_n n P_n$ and is also used for the resonator-drive calibration and Wigner tomography below. A representative swap trace and the extracted photon-number distribution are shown in Fig. S11.

C. Preparation of ground state

1. *Adiabatic preparation of eigenstates*

To resolve the low-lying spectral branches discussed in the main text, we prepare approximate eigenstates of the target Hamiltonian by adiabatically connecting simple product states to the interacting regime. The pulse sequence is summarized in Fig. S12. The sequence is organized into three experimental blocks: preparation and calibrated control pulses, photon-number and tomography mapping operations, and final measurement. In the preparation

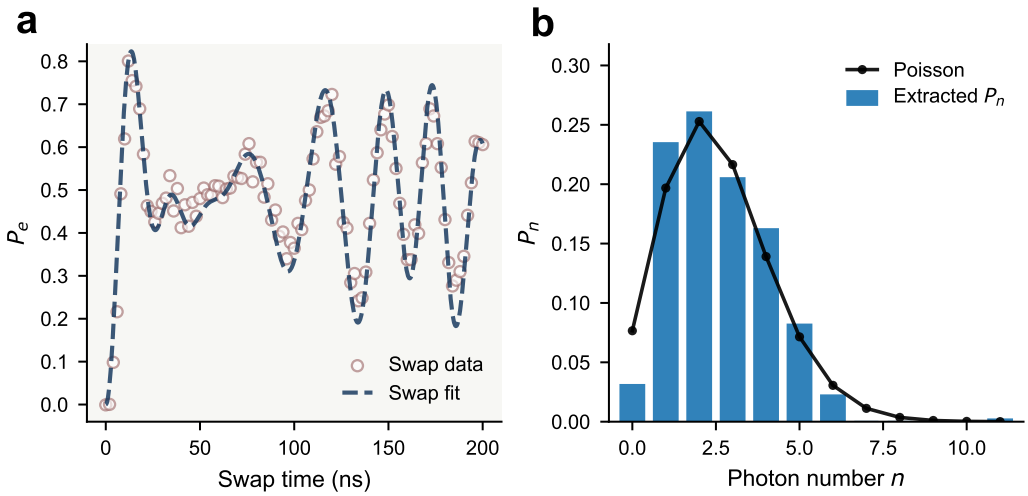

FIG. S11. **Photon-number-resolved resonator readout.** **a**, Representative resonant ancilla-resonator oscillation used to extract the photon-number distribution of the resonator state. The measured ancilla excitation probability is fitted with Eq. (S90). **b**, Extracted photon-number probabilities compared with a Poisson distribution with the same mean photon number, $\langle n \rangle = 2.57$.

block, the resonator is initialized close to $|0\rangle$ and the system qubit is prepared in either $|g\rangle$ or $|e\rangle$, corresponding to the two decoupled product states used to access the two lowest branches. The calibrated coupler-Z waveform then ramps the effective qubit-resonator coupling to the target value while the qubit and resonator control fields set the synthesized Hamiltonian parameters.

The ramp is described by

$$g_0(t) = g_0^{\mathrm{tar}} f(t/T_{\mathrm{ramp}}), \qquad f(0) = 0, \quad f(1) = 1, \tag{S91}$$

where g_0^{tar} is the target interaction strength and f is a smooth ramp envelope obtained from the inverse tunable-coupling calibration. In the experiment, T_{ramp} is chosen for each target g_0^{tar} by balancing nonadiabatic leakage and decoherence, with typical values in the range of 1–3 μs. After the ramp, the mapping block implements the joint readout basis: qubit rotations and resonator displacement pulses set the tomography basis, and the auxiliary-qubit–resonator interaction maps the photon-number populations onto the auxiliary qubit. The final measurement block records the corresponding qubit state by single-shot readout. The energy of the prepared branch is extracted from the reconstructed density matrix as

$$E_{\mathrm{exp}} = \mathrm{Tr}\left(\rho_{\mathrm{exp}} H_{\mathrm{tar}}\right), \tag{S92}$$

where ρ_{exp} is the reconstructed density matrix and H_{tar} is the target Hamiltonian at the final parameters.

The choice of ramp duration is guided by numerical simulations of the time-dependent effective Hamiltonian. For a target instantaneous eigenstate $|\psi_j(g_0^{\mathrm{tar}})\rangle$, we estimate the adiabatic-following fidelity

$$F_j^{\mathrm{ad}}(T_{\mathrm{ramp}}) = \left|\langle \psi_j(g_0^{\mathrm{tar}}) | \, \psi_j(T_{\mathrm{ramp}})\rangle\right|^2, \tag{S93}$$

where $|\psi_j(T_{\mathrm{ramp}})\rangle$ is the state obtained by evolving the corresponding decoupled product state under the ramped Hamiltonian. The ramp durations used in the measurements are

chosen in the plateau region of this numerical adiabatic-following estimate while remaining short compared with the relevant coherence times.

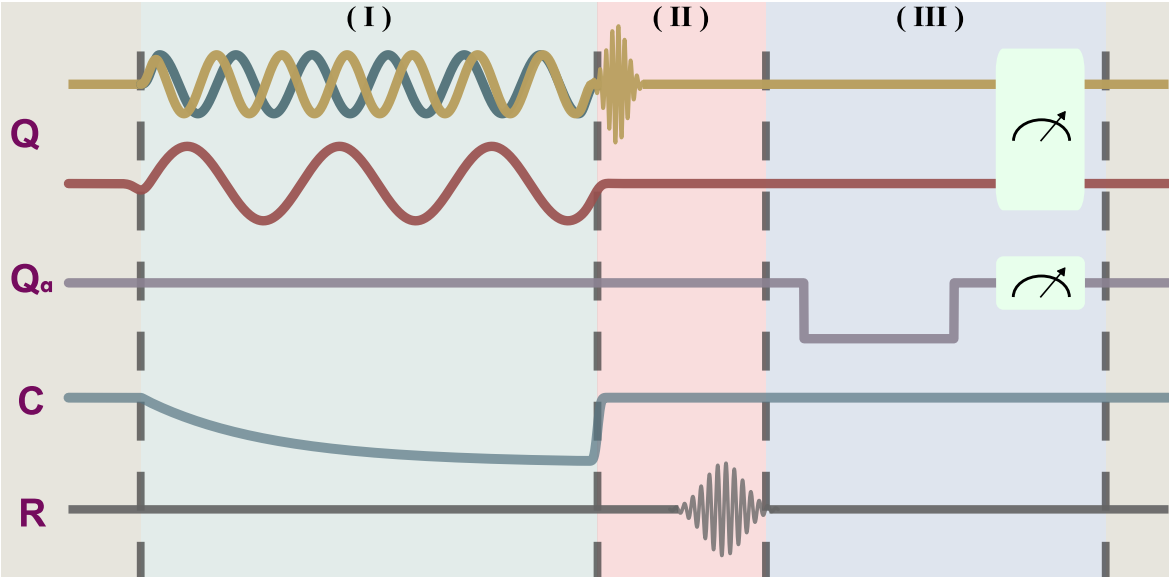

FIG. S12. **Adiabatic preparation of low-lying eigenstates.** **a**, Preparation and calibrated control pulses used to adiabatically connect decoupled product states to eigenstates of the target interacting Hamiltonian. The coupler-Z waveform implements the calibrated ramp $g_0(t)$, while the qubit and resonator control pulses set the effective Hamiltonian parameters. **b**, Mapping operations, including tomography rotations, resonator displacements, and ancilla-assisted photon-number mapping. **c**, Final measurement used to record the mapped qubit state.

2. *Joint qubit-resonator Wigner tomography*

We reconstruct the joint qubit-resonator density matrix using displacement-assisted tomography [16]. Before the photon-number-resolved readout, we apply a single-qubit rotation $U_i \in \{I, R_x(\pi/2), R_y(\pi/2)\}$ to the system qubit and a displacement operation $D(\alpha_j)$ to the resonator. The resonator displacement maps information about off-diagonal resonator matrix elements onto measurable photon-number populations, while the qubit rotations select different qubit-basis components. By choosing a set of displacement points $\{\alpha_j\}$ and measuring the corresponding qubit-conditioned photon-number populations, the original joint density matrix is reconstructed from an over-constrained set of equations via least-squares optimization.

Collecting the measured diagonal populations for all qubit rotations and resonator displacement points gives an over-constrained linear system,

$$\mathbf{y}_{\mathrm{exp}} = \mathcal{T}\mathbf{x}, \qquad \mathbf{x}_{\mathrm{LS}} = \arg\min_{\mathbf{x}} \|\mathcal{T}\mathbf{x} - \mathbf{y}_{\mathrm{exp}}\|_2^2 , \tag{S94}$$

where $\mathbf{x}$ is the vectorized joint density matrix and $\mathbf{y}_{\mathrm{exp}}$ contains the measured diagonal populations. In our measurements, the displacement points are chosen within a disk of radius $|\alpha| \leq 1$, with ten displacement amplitudes used in the reconstruction. The Wigner matrix shown in the main text is calculated from the reconstructed joint density matrix.

D. Tunneling dynamics associated with hidden symmetries

1. Preparation of displaced Fock states

The tunneling dynamics discussed in the main text is initialized in a product state of a displaced resonator state and a rotated qubit state. For the anisotropic case, the target initial state is

$$|\psi_{\mathrm{init}}^{(\lambda)}\rangle = D(-\alpha_\lambda)\,|0\rangle \otimes |+_\lambda\rangle\,, \qquad \alpha_\lambda = \frac{\sqrt{\lambda}g_1}{\omega}, \qquad |+_\lambda\rangle = \frac{\sqrt{\lambda}\,|g\rangle + |e\rangle}{\sqrt{1+\lambda}}. \tag{S95}$$

Starting from $|0, g\rangle$, the qubit component $|+_\lambda\rangle$ is prepared by a single-qubit rotation $R_y(\theta_\lambda)$ with

$$\theta_\lambda = 2\arctan\left(\frac{1}{\sqrt{\lambda}}\right), \tag{S96}$$

followed by a resonator displacement pulse implementing $D(-\alpha_\lambda)$. The parameterized rotation $R_y(\theta_\lambda)$ is implemented using the single-qubit gate decomposition described above.

The prepared state is verified by reconstructing the joint density matrix ρ_{exp} and evaluating

$$F_{\mathrm{init}} = \langle\psi_{\mathrm{init}}^{(\lambda)}|\,\rho_{\mathrm{exp}}\,|\psi_{\mathrm{init}}^{(\lambda)}\rangle\,. \tag{S97}$$

For visualization, we trace out the qubit degree of freedom,

$$\rho_R = \mathrm{Tr}_q(\rho_{\mathrm{exp}}), \tag{S98}$$

and calculate the reduced resonator Wigner function from the reconstructed ρ_R. The reconstructed resonator Wigner functions and qubit Bloch vectors are shown in Fig. S13.

2. Readout of displaced Fock states

The populations in the tunneling basis are measured by applying a state-mapping operation before the standard joint readout. For a target tunneling-basis state

$$|\psi_{\mathrm{tar}}\rangle = \mathcal{U}_{\mathrm{map}}\,|n, m\rangle\,, \tag{S99}$$

where $|n, m\rangle$ denotes the product state of a bare resonator Fock state $|n\rangle$ and a qubit state $|m\rangle$ with $m \in \{g, e\}$, the population at time t is

$$P_{\psi_{\mathrm{tar}}}(t) = \langle n, m|\,\mathcal{U}_{\mathrm{map}}^\dagger \rho(t) \mathcal{U}_{\mathrm{map}}\,|n, m\rangle\,. \tag{S100}$$

Experimentally, this population is obtained by applying $\mathcal{U}_{\mathrm{map}}^\dagger$ before the joint readout. Here $\mathcal{U}_{\mathrm{map}}^\dagger$ consists of the inverse resonator displacement and the inverse qubit rotation. The population in the tunneling-basis state is then extracted from the photon-number-resolved resonator readout combined with the qubit-state readout.

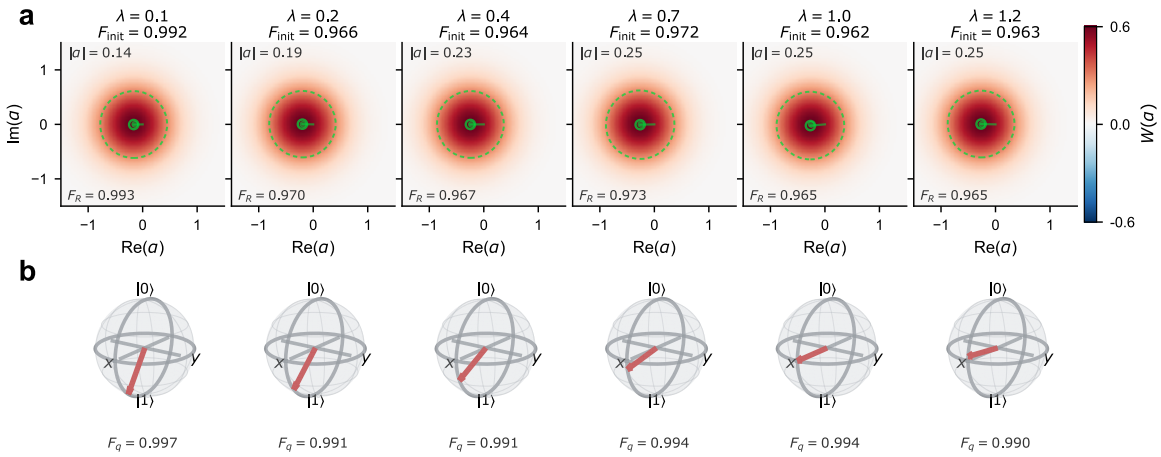

FIG. S13. **Preparation and verification of tunneling-basis initial states.** **a**, Reduced resonator Wigner functions reconstructed from $\rho_R = \mathrm{Tr}_q(\rho_{\mathrm{exp}})$ for different anisotropy ratios λ. The resonator displacement is set by $|\alpha_\lambda| = \sqrt{\lambda} g_1/\omega$; the marked centers and contours indicate the reconstructed phase-space displacement. **b**, Qubit Bloch vectors reconstructed from the reduced qubit density matrices, with components $x = \mathrm{Tr}(\rho_q \hat{\sigma}_x)$, $y = \mathrm{Tr}(\rho_q \hat{\sigma}_y)$, and $z = \mathrm{Tr}(\rho_q \hat{\sigma}_z)$. The quoted fidelities are the joint initial-state fidelities $F_{\mathrm{init}} = \langle \psi_{\mathrm{init}}^{(\lambda)} | \, \rho_{\mathrm{exp}} \, | \psi_{\mathrm{init}}^{(\lambda)} \rangle$, together with the reduced-state fidelities F_R and F_q.

[1] Q.-T. Xie, S. Cui, J.-P. Cao, L. Amico, and H. Fan, Anisotropic Rabi model, Phys. Rev. X **4**, 021046 (2014).
[2] Z.-M. Li and M. T. Batchelor, Hidden symmetry and tunneling dynamics in asymmetric quantum Rabi models, Phys. Rev. A **103**, 023719 (2021).
[3] V. V. Mangazeev, M. T. Batchelor, and V. V. Bazhanov, The hidden symmetry of the asymmetric quantum Rabi model, J. Phys. A: Math. Theor. **54**, 12LT01 (2021).
[4] C. Reyes-Bustos, D. Braak, and M. Wakayama, Remarks on the hidden symmetry of the asymmetric quantum Rabi model, J. Phys. A: Math.Theor. **54**, 285202 (2021).
[5] D. Ballester, G. Romero, J. J. García-Ripoll, F. Deppe, and E. Solano, Quantum simulation of the ultrastrong-coupling dynamics in circuit quantum electrodynamics, Phys. Rev. X **2**, 021007 (2012).
[6] P. Forn-Díaz, L. Lamata, E. Rico, J. Kono, and E. Solano, Ultrastrong coupling regimes of light-matter interaction, Rev. Mod. Phys. **91**, 025005 (2019).
[7] A. Blais, A. L. Grimsmo, S. Girvin, and A. Wallraff, Circuit quantum electrodynamics, Rev. Mod. Phys. **93**, 025005 (2021).
[8] F. Yan, P. Krantz, Y. Sung, M. Kjaergaard, D. L. Campbell, T. P. Orlando, S. Gustavsson, and W. D. Oliver, Tunable coupling scheme for implementing high-fidelity two-qubit gates, Phys. Rev. Appl. **10**, 054062 (2018).
[9] H. Lignier, C. Sias, D. Ciampini, Y. Singh, A. Zenesini, O. Morsch, and E. Arimondo, Dynamical control of matter-wave tunneling in periodic potentials, Phys. Rev. Lett. **99**, 220403 (2007).
[10] Y.-H. Shi, Y. Liu, Y.-R. Zhang, *et al.*, Quantum simulation of topological zero modes on a 41-qubit superconducting processor, Phys. Rev. Lett. **131**, 080401 (2023).
[11] Y. Liu, Y.-R. Zhang, Y.-H. Shi, *et al.*, Interplay between disorder and topology in Thouless pumping on a superconducting quantum processor, Nat. Commun. **16**, 108 (2025).
[12] J. Casanova, G. Romero, I. Lizuain, J. J. García-Ripoll, and E. Solano, Deep strong coupling regime of the Jaynes-Cummings model, Phys. Rev. Lett. **105**, 263603 (2010).
[13] D. Braak, Integrability of the Rabi model, Phys. Rev. Lett. **107**, 100401 (2011).
[14] S. Krinner, S. Storz, P. Kurpiers, P. Magnard, J. Heinsoo, R. Keller, J. Lütolf, C. Eichler, and A. Wallraff, Engineering cryogenic setups for 100-qubit scale superconducting circuit systems, EPJ Quantum Technol. **6**, 2 (2019).
[15] D. C. McKay, C. J. Wood, S. Sheldon, J. M. Chow, and J. M. Gambetta, Efficient Z gates for quantum computing, Phys. Rev. A **96**, 022330 (2017).
[16] X. Y. LinPeng, H. Z. Zhang, K. Xu, C. Y. Li, Y. P. Zhong, Z. L. Wang, H. Wang, and Q. W. Xie, Joint quantum state tomography of an entangled qubit–resonator hybrid, New J. Phys. **15**, 125027 (2013).